ANIMAL ROBOTS

Tuna robotics: A high-frequency experimental platform exploring the performance space of swimming fishes

J. Zhu[1], C. White[1], D. K. Wainwright[2], V. Di Santo[2]*, G. V. Lauder[2], H. Bart-Smith[1]†

Tuna and related scombrid fishes are high-performance swimmers that often operate at high frequencies, especially during behaviors such as escaping from predators or catching prey. This contrasts with most fish-like robotic systems that typically operate at low frequencies (< 2 hertz). To explore the high-frequency fish swimming performance space, we designed and tested a new platform based on yellowfin tuna (*Thunnus albacares*) and Atlantic mackerel (*Scomber scombrus*). Body kinematics, speed, and power were measured at increasing tail beat frequencies to quantify swimming performance and to study flow fields generated by the tail. Experimental analyses of freely swimming tuna and mackerel allow comparison with the tuna-like robotic system. The Tunabot (255 millimeters long) can achieve a maximum tail beat frequency of 15 hertz, which corresponds to a swimming speed of 4.0 body lengths per second. Comparison of midline kinematics between scombrid fish and the Tunabot shows good agreement over a wide range of frequencies, with the biggest discrepancy occurring at the caudal fin, primarily due to the rigid propulsor used in the robotic model. As frequency increases, cost of transport (COT) follows a fish-like U-shaped response with a minimum at ~1.6 body lengths per second. The Tunabot has a range of ~9.1 kilometers if it swims at 0.4 meter per second or ~4.2 kilometers at 1.0 meter per second, assuming a 10–watt-hour battery pack. These results highlight the capabilities of high-frequency biological swimming and lay the foundation to explore a fish-like performance space for bio-inspired underwater vehicles.

INTRODUCTION

Robotic platforms designed to emulate aquatic locomotion have typically focused on lower-frequency swimming, replicating the basic undulatory body and fin kinematics of fishes when they swim slowly (*1–7*). Efforts to recreate fish propulsion using an undulating and deformable body have shown some success (*3, 8–12*), and yet there is still much to learn from biology to successfully implement solutions that can closely match the performance of high-speed biological systems. In contrast to the majority of fish-like robotic systems, fishes exhibit a wide range of tail beat frequencies and swimming speeds (Fig. 1). Undulatory body propulsion is a versatile locomotor system; a single fish species may exhibit a range of tail beat frequencies from 0.1 to beyond 20 Hz, resulting in swimming speeds surpassing 20 body lengths per second (BL/s) (*13–17*). Although fishes occupy this large performance space, current robotic fish designs are unable to achieve both high-frequency movements and high swimming speeds while maintaining energetic costs that are reasonable from a biological perspective (Fig. 1).

Bio-inspired systems designed to push into regions of higher frequency and speed will require knowledge of biological features that promote high performance, and these features should then be implemented in designs to improve speed, economy, and efficiency. Whereas biology can inspire a high-performance robotic platform, development of such a platform will also provide an opportunity to experimentally study both high-speed swimming and the function of features unique to high-performance fishes. This feedback loop between bio-inspired robotics and robotics-inspired biology (*18*) creates a framework for combining biological features into a robotic platform to optimize performance in ways that may eventually surpass biological function. Designing fish-inspired platforms that are capable of high-performance swimming is therefore crucial for expanding the capabilities of nontraditional propulsors in both a utilitarian and a scientifically relevant way.

Many fishes swim by oscillating their body and tail to generate a wave of bending that passes along the body from head to tail. This undulatory body propulsion produces thrust by accelerating water, which is then shed from the tail trailing edge (*19–23*). The amplitude of this undulatory wave increases from head to tail, resulting in wave speeds greater than the forward swimming speed of the fish. As a consequence, slip values—the ratio of swimming speed U to wave speed V (U/V)—range between 0.4 and 0.8 (*15, 24–28*). This propulsive body wave typically generates a fluid wake that is a reverse Kármán street, with a central high-velocity fluid jet directed opposite to the path of body motion and bordered by counter-rotating vortices that are shed as the tail changes direction at peak amplitude. Increasing the frequency of body waves also increases both the speed of the thrust jet and the shedding frequency of the vortices at the tail, resulting directly in faster swimming speed. In this way, fish swimming speed is largely modulated by frequency [and often at a specific ratio of wavelength to tail amplitude (*29*)], and changing frequency allows fish velocity to range from near zero to more than 20 BL/s (Fig. 1). The relationship between tail beat frequency and velocity is often evaluated using the stride length—the distance moved by the body (length, L) during one tail beat. This can vary from 0.25 L during slow speed movements to about 1.0 L by tuna-like fish swimmers (*13, 14, 30*).

A number of robotic models have been developed to mimic various aspects of fish swimming dynamics, and these efforts varied from models of single fins (*31, 32*) to whole-body fish-like systems with mechanical components to deform the body and generate a propulsive wave (*3, 33, 34*). Some fish-like robotic systems were free swimming (*1, 35, 36*), whereas others were attached to external force transducers and/or power supplies, which allow quantitative

[1]Bio-Inspired Engineering Research Laboratory (BIERL), Department of Mechanical and Aerospace Engineering, University of Virginia, 122 Engineer's Way, Charlottesville, VA 22903, USA. [2]Museum of Comparative Zoology, Harvard University, 26 Oxford Street, Cambridge, MA 02138, USA.
*Present address: Stockholm University, Department of Zoology, Svante Arrhenius väg 18 B, 106 91 Stockholm, Sweden.
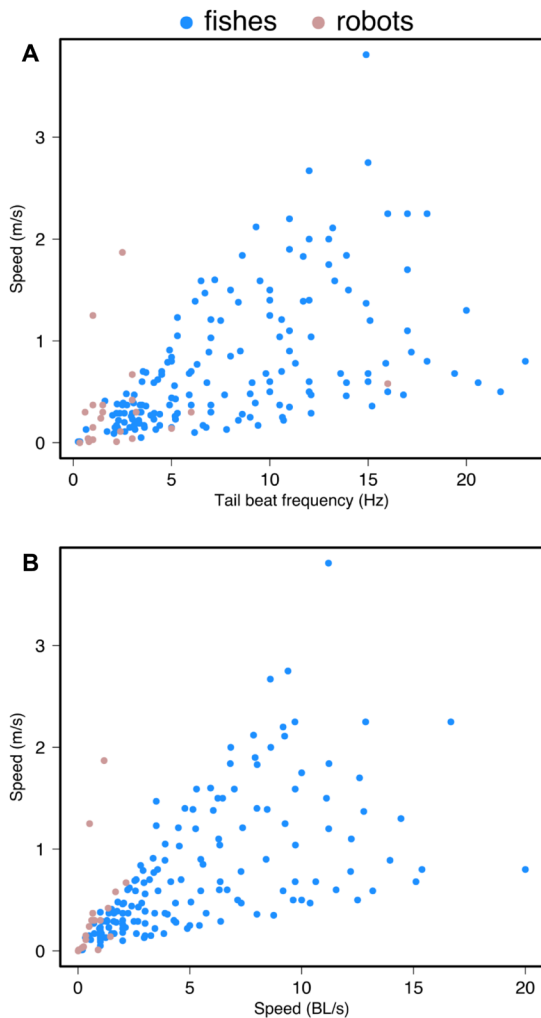†Corresponding author. Email: hb8h@virginia.edu

Fig. 1. Locomotor performance space of swimming fishes and robots. Fishes are capable of locomotion at much higher speeds and frequencies than most current robotic systems. Current fish-like robotic platforms (pink dots) occupy only a small region of the fish swimming performance space (blue dots) considering both speed and tail beat frequency (**A**), and absolute and length-specific speeds (**B**). Points represent literature data from different robotic platforms, literature data for multiple individuals of one fish species [e.g., (*17*)], or new measurements of fish swimming speeds and tail beat frequencies conducted by the authors.

evaluation of swimming performance and calculation of the cost of transport (COT) (*37*, *38*). In addition, several efforts closely mimicked the morphology of fish and attempted to replicate swimming kinematics (*39–42*); others were "fish like" but were not directly comparable with any particular species and used either elongated undulating fins or flapping foils actuated in heave, pitch, or both to generate thrust during swimming (*1*, *35*, *42–46*). Last, most fish-like robotic systems operated in the frequency range of 0.25 to 3 Hz and achieved body velocities of ~0.25 to 1.5 BL/s (Fig. 1) (*1*, *2*, *5*, *6*). A few platforms have extended the range of operating frequencies above 3 Hz [e.g., (*42*, *44*)]; however, swimming speeds at these higher frequencies were often less than 1 BL/s, and power consumption was high [e.g., 16 Hz, 0.8 BL/s, and 20 W in (*44*)]. Reports of power consumption and measurements of the COT over a range of frequencies are unexpectedly uncommon in fish robotics [but see (*35*)], although such data are

particularly valuable for comparison to energetic data obtained from swimming fishes.

Scombrid fishes (family Scombridae), which include tunas and mackerels, provide an ideal group in which to study high-performance locomotor behaviors. They exhibit a number of morphological adaptations for high-speed and high-endurance swimming (*16*, *47–51*), including a high–aspect ratio tail, a narrow pre-tail (or peduncle) region, and a large locomotor muscle mass to produce high-frequency tail beats and hence high-speed locomotion. Robotic systems based on scombrid fishes should therefore be able to extend current fish-like robotic locomotion into a higher performance realm. To this end, the goals of this study were (i) to develop and test a fish-like robotic platform (on the order of 30 cm in length) that can achieve tuna-like tail beat frequencies up to 15 Hz and produce swimming speeds of 3 to 4 BL/s; (ii) to evaluate the swimming performance of this platform by quantifying kinematics, power consumption, COT, and fluid flow produced by the tail during swimming; and (iii) to compare qualitatively and quantitatively the kinematic performance of this platform with new kinematic data obtained from freely swimming tuna and mackerel.

RESULTS
Tunabot platform design
A major focus of this study was the development of a tuna-like robotic platform with tail beat frequency, stride length, and COT curve comparable to that of thunniform fish. To achieve these performance metrics, we developed the Tunabot to approximate the overall body shape, kinematics, swimming speeds, and power consumption curves of scombrid fishes. The external design of the Tunabot platform was inspired by computed tomography (CT) scans of yellowfin tuna (*Thunnus albacares*), and the size of the platform is similar to adult-sized Atlantic mackerel (*Scomber scombrus*) or young yellowfin tuna (Fig. 2). The Tunabot measures 255.3 mm in length, 49.2 mm in width, and 67.8 mm in height and has three main sections, namely, a head assembly, a central actuating region, and a peduncle-caudal fin assembly (Fig. 2A). It has a mass of 0.306 kg in air. Details of the Tunabot design and construction are provided in Materials and Methods.

The Tunabot body reflects a simplified version of scombrid fish morphology, where all fins were removed except the tail (compare Fig. 2, B and C). We focused on the role of the body and tail in propulsion to help identify fundamental contributions of these components to locomotor performance. The external shape of the Tunabot tail and peduncle region was based on the morphology of yellowfin tuna and includes a high–aspect ratio tail, a narrow peduncle, and lateral keels at the peduncle (Fig. 2, D to G). In contrast to the multiple intervertebral joints that allow lateral bending of the tail in scombrid fishes (*16*, *48*, *52*), we simplified the Tunabot tail design by using a single mechanical joint that connects a rigid keel to the caudal fin (there is an actuated joint just posterior to midlength on the Tunabot body; details are found in Materials and Methods). This engineering simplification allows for a simpler, robust design with more predictable tail kinematics. In the Tunabot, the peduncle joint was free to rotate between symmetric limits of 18° about the neutral axis. Two elastic bands were attached from the keel to the caudal fin (Fig. 2G), which act like the longitudinal tendons in scombrid fishes (*47*, *52*, *53*) and give the tail joint rotational stiffness. The caudal fin was three-dimensional (3D)–printed from VeroWhite
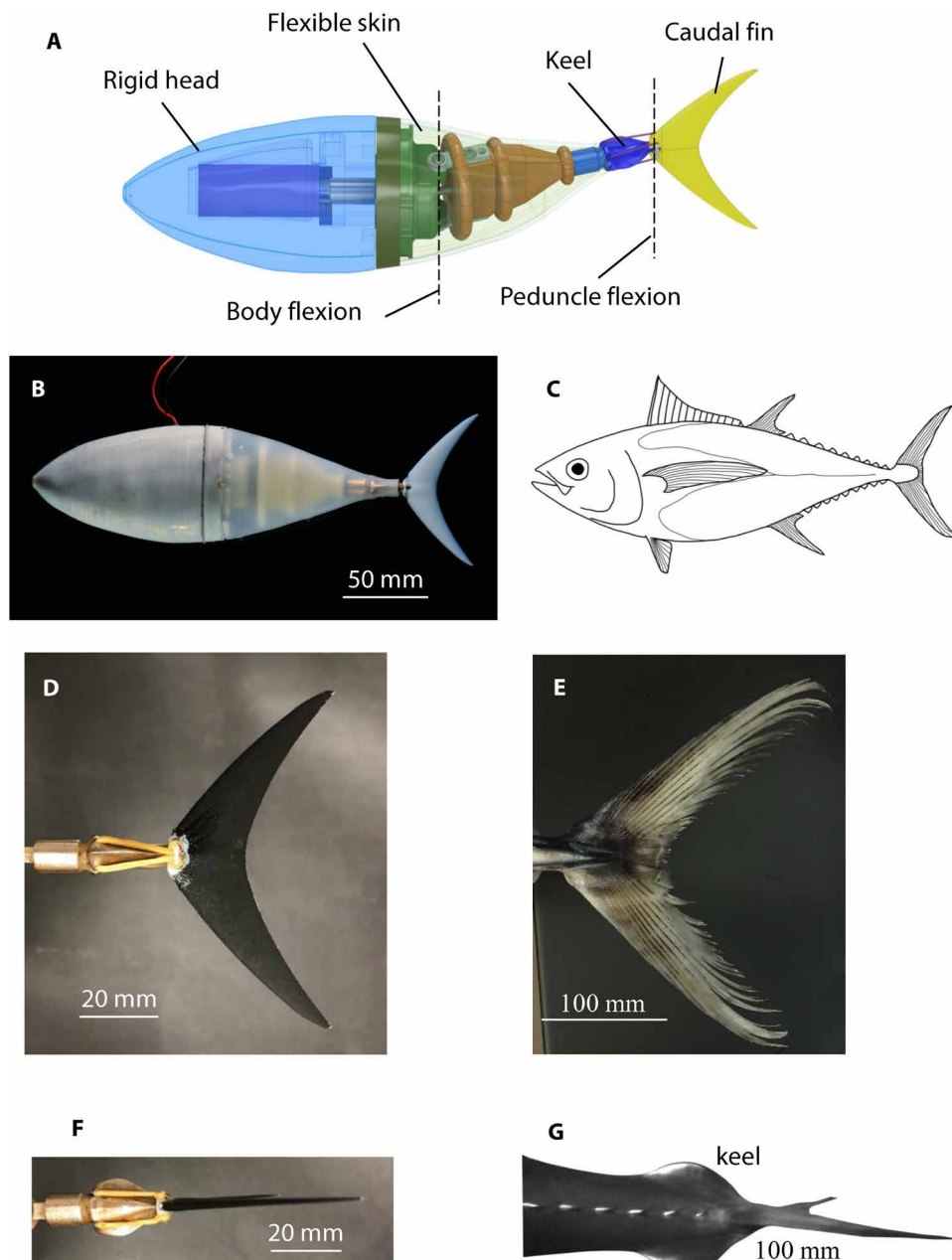
Fig. 2. Design of the Tunabot platform. (**A**) Overall Tunabot body plan showing the major components of the tuna-like mechanical system. The Tunabot is 255 mm in total length. Body shape (**B**) was based on a simplified yellowfin tuna (*T. albacares*) body plan (**C**) and features a streamlined shape with a narrow caudal peduncular region anterior to the tail. During testing, the Tunabot was suspended by two thin vertical threads, and one lateral thread at the nose prevented extreme motion in the event of failure but did not restrict lateral Tunabot oscillation during swimming. The power cable (red) is visible and also did not restrict robot motion in any way. Tunabot tail morphology (**D**) was manufactured on the basis of the yellowfin tuna tail (**E**). The tail is supported by a metal peduncle with lateral keels (**F**) designed from the lateral keels of yellowfin tuna (**G**). Images of tuna in (**E**) and (**G**) are from a fish about 1 m in length.

Supplementary Materials, as are videos of Tunabot (movies S3 and S4), yellowfin tuna (movie S1), and mackerel (movie S2) swimming.

During testing, the Tunabot was supported by three thin threads (one lateral and two vertical) attached to the robot. The two vertical threads supported the negatively buoyant robot in the center of the flow tank, whereas the third thread loosely attached to the side of the robot and did not support or restrict the movement of the robot. This side thread can be seen in Fig. 3A and functioned to prevent extreme motions in the event of mechanical failure or flow perturbations introduced during speed changes. Tunabot center-of-mass motion was thus unconstrained in the streamwise and lateral directions. A power cable allowing external control was also loose and did not support the Tunabot (Fig. 2B) or restrict lateral motion.

Midline kinematics

Midlines for the swimming Tunabot (Fig. 3A), yellowfin tuna (Fig. 3B), and mackerel (Fig. 3C) are shown in Fig. 3, D to F, and these midlines correspond to swimming speeds of 2.2, 1.0, and 2.0 BL/s, respectively. Using these midlines, we calculated curvature along the body length (Fig. 3, G to I) normalized by overall body length. The locations of peak curvature in the Tunabot, yellowfin tuna, and mackerel (Fig. 2, G to I) correspond to the locations of maximal body and caudal fin flexion. Average curvature gradually increases along the body in tuna and mackerel, which is consistent with previous biological observations in other swimming fishes (*25, 54–56*). Both mackerel and tuna show the highest curvatures in the caudal fin region, reflecting flexibility of this propulsive surface. In contrast, the Tunabot shows peak curvature at 0.8 BL, which is the location of the peduncular joint where tail oscillation occurs. The stiff manufactured tail of the Tunabot results in minimal curvature in the most posterior body regions, thus resulting in a body curvature profile that differs in this location from that of yellowfin tuna and mackerel.

Midline data also allow quantification of the lateral (side to side) amplitude of head and caudal fin excursion from the midline mean direction of travel. Head and tail oscillation amplitudes of the Tunabot are 0.05 and 0.15 BL, respectively. Comparable values are 0.05 and 0.20 BL for yellowfin tuna and 0.04 and 0.23 BL for mackerel.
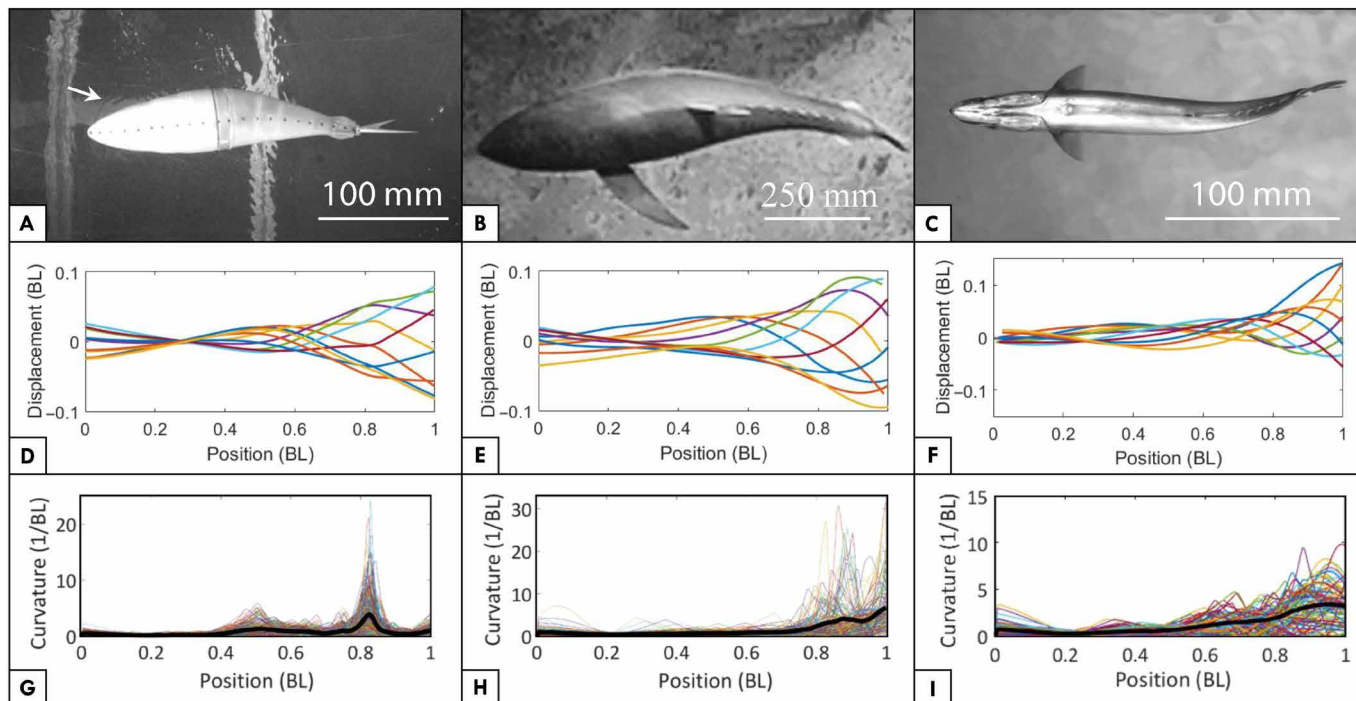
resin material, with a chordwise cross section of a NACA 0016 profile airfoil. The final design captures the key morphological features of scombrid fish propulsive systems: posterior intervertebral joints, lateral keels, a narrow peduncle, lateral tendons, and a stiff, high–aspect ratio caudal fin. More details of the design and construction, including waterproofing and testing protocols, are given in the

Fig. 3. Swimming kinematics. (**A**) Tunabot, (**B**) Yellowfin tuna, and (**C**) mackerel. Kinematic snapshots showing the displacement of the body midline at 10 equally spaced time intervals during a single tail beat cycle (**D** to **F**) during swimming at 2.2, 1.0, and 2.0 BL/s, respectively. We calculated midline curvature along the body for 270, 168, and 85 midlines, corresponding to 27, 15, and 7 tail beats (**G** to **I**), respectively. Black lines (G to I) show the mean body curvature. Tuna in (B) is about 1 m in length. The negatively buoyant Tunabot in (A) was supported by two vertical threads (not visible in this image), and a thin black lateral thread was loosely attached to the nose (visibly attached to near the first black dot) to prevent potentially damaging movements. This thread did not restrict lateral movement of the robot in any way.

The reduced caudal fin excursion of the Tunabot is attributed to the high stiffness of the propulsor. The Tunabot has a rigid caudal fin, whereas mackerel and tuna caudal fins are flexible, resulting in an increase in tail tip amplitude in tuna and mackerel relative to that in the Tunabot.

Figure 4 compares an analysis of the caudal fin angle of attack for the Tunabot swimming at 0.8 BL/s with a tail beat frequency of 3.7 Hz (Fig. 4A) with similar data measured from swimming mackerel (Fig. 4B). Mackerel tails are flexible during propulsion, and hence, we report the angle of attack over four different regions of the caudal fin (Fig. 4B). As the Tunabot's tail oscillates from side to side (Fig. 4A), it reaches a high effective angle of attack of nearly ±50°. This is in contrast to the mackerel tail, which maintains an angle of attack of about ±20°, except when tail beat direction changes and angle of attack is momentarily as high as 50°. Extreme effective angles of attack for both the Tunabot and mackerel occur midstroke when the caudal fin passes the body's center line. This corresponds to the middle of the "Right Stroke" and "Left Stroke" shaded regions in Fig. 4. The high effective angle of attack values for the Tunabot's tail are mostly outside the range of ±25° and are therefore where dynamic stall occurs in similarly shaped airfoils (*57, 58*). Dynamic stall produces leading-edge vortices (LEVs), allowing lift generation past static stall angles of attack, and is well documented in fish locomotion and insect flight (*18, 59–63*). A high lift force generated by dynamic stall produces higher lateral force on the caudal fin, which in turn causes a higher ratio of head oscillation amplitude to tail oscillation amplitude in the Tunabot. Conversely, each of the mackerel's four tail segments has an effective angle of attack within the optimal range (described further in Materials and Methods) where dynamic stall is unlikely to be present except during the transitions between tail beat directions. During these transitions, only some segments of the caudal fin have effective angles of attack inside the optimal range. The similarity in angles between each segment is remarkable considering the mackerel's high caudal fin curvature (Fig. 3I). Thus, the Tunabot's range of attack angles for the caudal fin exceeds that of the mackerel by about 20° and is well outside of the optimal range for about half the beat period. We estimated that maximal thrust occurs at the midstroke tail position when the tail crosses the mean path of motion. For mackerel, all four caudal fin segment angles converge midstroke, suggesting that the effective angle of attack is uniform over the entire length of the mackerel's caudal fin. The range in angles cyclically decreases toward midstroke and increases toward midtransition.

At the same tail beat frequency (3.5 Hz), mackerel swim nearly twice as fast as the Tunabot, which indicates overall greater thrust output. This is supported by differences in stride length. The Tunabot has stride lengths of 0.21, 0.3, and 0.32 BL at 0.8, 1.6, and 3.2 BL/s, respectively. In contrast, yellowfin tuna and mackerel have relatively longer stride lengths of 0.52 and 0.47 BL at swim speeds of 1.0 and 1.3 BL/s.

Thrust measurements of the Tunabot at a 3.5-Hz tail beat frequency (Fig. 4C) show that there are two thrust peaks for every complete tail beat, with maximal thrust occurring when the tail reaches its maximum effective angle of attack. At the points of maximal lateral tail excursion, however, the Tunabot produced low thrust because of low relative fin fluid velocity.
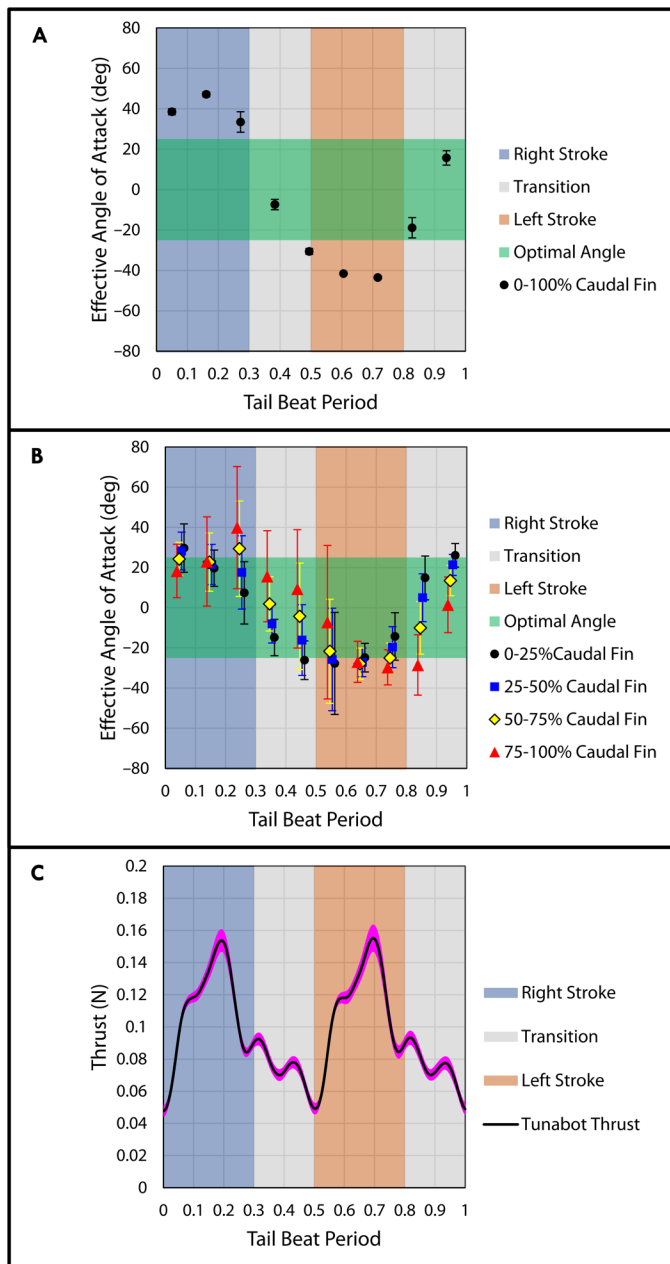
Fig. 4. Tail kinematics and thrust in the Tunabot and swimming mackerel. (**A**) Effective angle of attack profile for the Tunabot caudal fin over one tail beat period during locomotion at 0.78 ± 0.2 BL/s and a tail beat frequency of 3.7 ± 0.2 Hz ($n = 3$). The rigid caudal fin is treated as a single segment. Error bars indicate SD. (**B**) Effective angle of attack profiles for the mackerel caudal fin, with each profile representing a quarter segment of the caudal fin, as seen in ventral view. These data are from mackerel swimming at 1.2 ± 0.1 BL/s with a tail beat frequency of 3.7 ± 0.9 Hz ($n = 20$). (**C**) Static thrust of the Tunabot measured at a tail beat frequency of 3.9 ± 0.1 Hz ($n = 9$), represented with 95% confidence level. Two thrust peaks are evident for each complete tail beat cycle.

Frequency, speed, and COT

Figure 5 summarizes the comparison between swimming speed and tail beat frequency for the Tunabot compared with both new data on yellowfin tuna and literature data from a diversity of swimming fishes. We measured tuna tail beat frequency during both routine
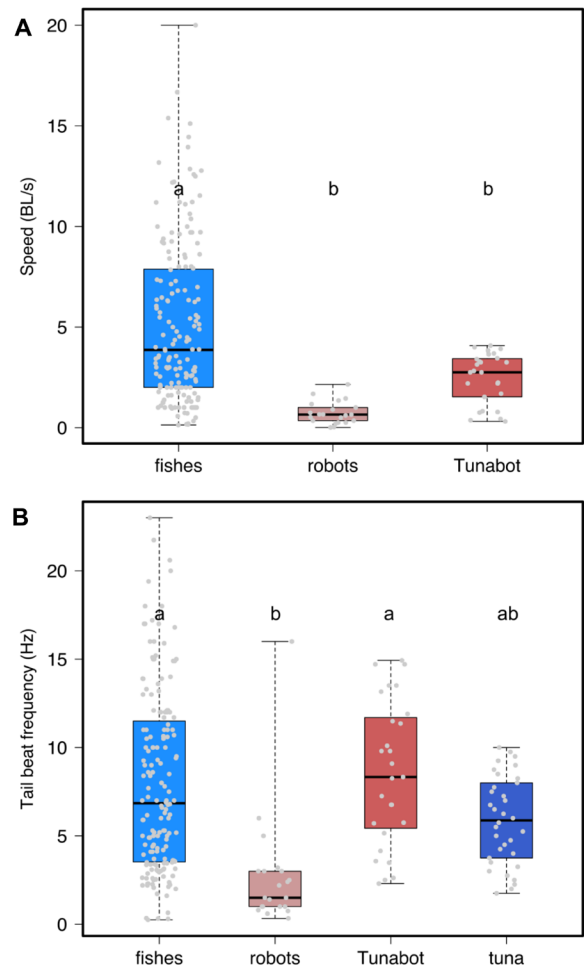

Fig. 5. Comparison of Tunabot swimming performance with fishes and other fish robotic platforms. (**A**) Swimming speeds (in body lengths per second) compared for swimming fish, fish-like robotic systems, and the Tunabot. (**B**) Tail beat frequencies (in hertz) compared for swimming fish, fish-like robotic systems, the Tunabot, and yellowfin tuna. Black horizontal lines indicate the group medians, colored boxes indicate the lower and upper data quartiles (25 and 75% levels), and dashed lines indicate the minimum and maximum data values for each group. The Tunabot has significantly higher tail beat frequencies than other fish-like robotic platforms ($P < 0.001$) and a higher length-specific swimming speed. Lowercase letters indicate significant differences among group means.

steady swimming and feeding bouts, which demonstrated that tunas can easily achieve a range of tail beat frequencies from 3 to 10 Hz. The Tunabot achieved a maximum tail beat frequency of 15 Hz, exceeding the maximum of 10 Hz that we recorded for larger (1 m long) tuna during feeding bouts. With one exception (*44*), the maximum Tunabot tail beat frequency exceeded measured frequencies from previous fish-like robotic platforms (Fig. 5B). Tunabot swimming speed is nearly linearly proportional to tail beat frequency (Fig. 6A), and the reduction in gradient above 10 Hz is attributable to slightly reduced caudal fin amplitude at higher frequencies. In addition, mean swimming speeds for the Tunabot over all frequencies were comparable to literature data for swimming fishes and greater than previously reported swim speeds for fish-like robots (Fig. 5A).

COT is defined as the ratio of power consumption to swimming speed, given as energy consumed to travel a unit distance. For the Tunabot, power consumption is the total input electrical power to
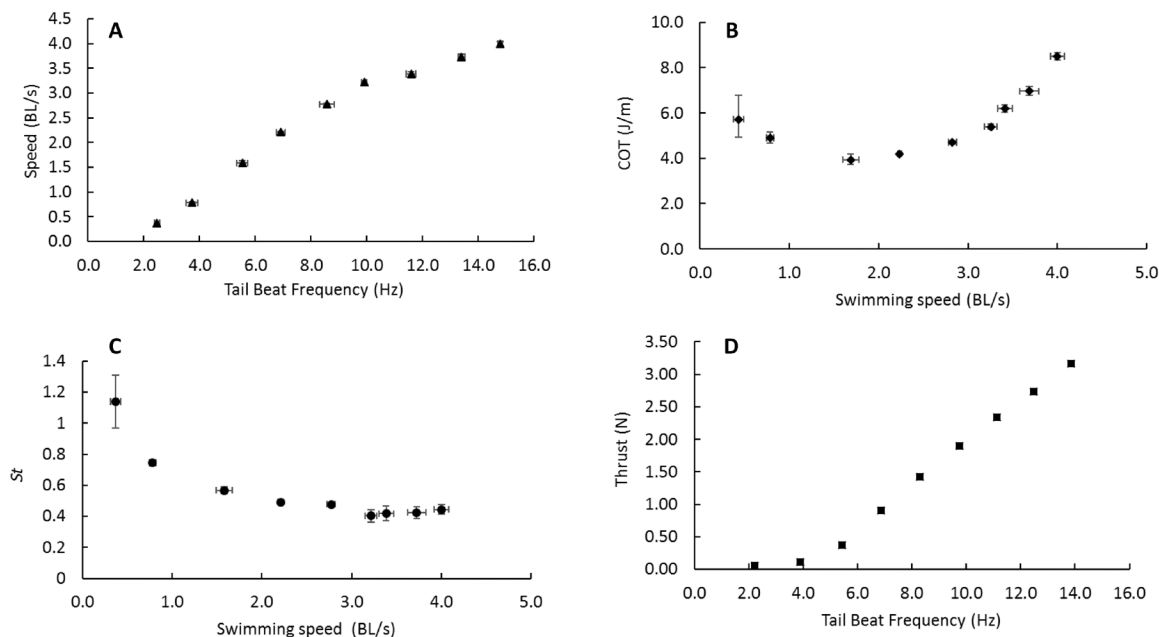
Fig. 6. Tunabot swimming performance. (**A**) Swimming speed versus tail beat frequency. (**B**) COT in joules per meter versus swimming speed given in body lengths per second. (**C**) St versus swimming speed. (**D**) Measured static thrust (in newtons) versus tail beat frequency (in hertz). Points are the means of $n = 3$ trials; error bars are SDs from the means. Error bars are obscured by the symbols for some points.

the DC motor, which we consider analogous to the metabolic power of fish. The Tunabot has a U-shaped COT relationship with swimming speed (Fig. 6B), where COT is higher at both low and high speeds compared with intermediate speeds. At 1.6 BL/s, the Tunabot reaches its lowest COT of 3.9 J/m. COT data for tuna and other fishes show similar U-shaped relationships with swimming speed and have minimum COTs that occur at similar speeds (*64, 65*). However, the minimum COT for swimming tuna is lower than that of the Tunabot (0.44 J/m at 1.2 BL/s).

The Strouhal number (*St*) is defined as $St = \frac{fA}{U}$, where *f* is the tail beat frequency, *A* is the peak-to-peak tail beat amplitude, and *U* is the swimming speed. The Tunabot's *St* decreased with swimming speed (Fig. 6C). At a swimming speed of 3.2 BL/s, the Tunabot's *St* reached its minimum of 0.4, which is close to the upper bound of optimality for flying and swimming animals (*66*). Thrust measurements for the Tunabot (Fig. 6D) show that thrust is linearly related to tail beat frequency except for low frequencies where thrust is negligible.

Caudal fin wake flow patterns
Flow visualization around the caudal fin and in the wake of the Tunabot was performed to assess its similarity to previously published wakes of freely swimming fishes and to examine the possibility of LEV generation by the oscillating tuna-like caudal fin (Fig. 7). Particle image velocimetry visualization was conducted at two locations on the tail: the center of the tail (Fig. 7A) and at 50% of the ventral fin span (Fig. 7B). All swimming speeds exhibited a reverse Kármán street wake characteristic of swimming fishes (Fig. 7C), and all swimming speeds also showed the development of an LEV on the caudal fin as the tail beats toward the midline (Fig. 7, D and E). The LEV is present during the time that the caudal fin makes a positive angle of attack to incident flow (Fig. 7E), and hence, we expect that the LEV contributes to thrust.

DISCUSSION
In designing the fish-inspired Tunabot, we were able to replicate several key anatomical features of high-performance scombrid fishes and extend fish-like robotic swimming performance into the higher-frequency performance space occupied by fishes (Figs. 1 and 5). We used the Tunabot to (i) compare and contrast locomotor performance with yellowfin tuna and Atlantic mackerel thunniform swimmers and (ii) explore the performance of high-frequency swimming as it pertains to speed and COT. The Tunabot was able to replicate the U-shaped COT curve (Fig. 5B) found in many fishes (*15, 67–70*) with a minimum cost at an intermediate swimming speed. Fish often display increased swimming costs at the low speeds, and in some cases, energetic data have shown that the absolute cost of swimming (expressed as energy per unit time only) is also higher at the lowest swimming speeds (*65, 69*). As speed increases, energetic costs increase also. At its minimum COT, the Tunabot swims at 1.6 BL/s and has a range of ~9.1 km if it swims at 0.4 m/s or ~4.2 km at 1.0 m/s, assuming a 10–watt-hour (Wh) battery pack that could be installed in the nonbending head region.

Previous research has shown a decreasing *St* as fishes increase swimming speed (*71*), and the Tunabot replicated this pattern and reached a plateau *St* near 0.4 at speeds above 3.2 BL/s (Fig. 6C). This value is near the upper limit of the *St* range (0.2 to 0.4) considered typical for undulatory fish swimming (*71–74*). A lower *St* for the Tunabot could be achieved by redesigning the Tunabot to have an increased tail beat amplitude and a lower effective angle of attack of the tail—achievable in part by introducing flexibility in the caudal fin. In the current Tunabot design, the tail beat amplitude is somewhat reduced compared with that in swimming tuna and mackerel (Fig. 3), and the tail's angle of attack reaches higher values than those we measured for swimming scombrid fishes (Fig. 4).

Swimming speed in the Tunabot follows a roughly linear relationship with tail beat frequency (Fig. 6A), which is also true for
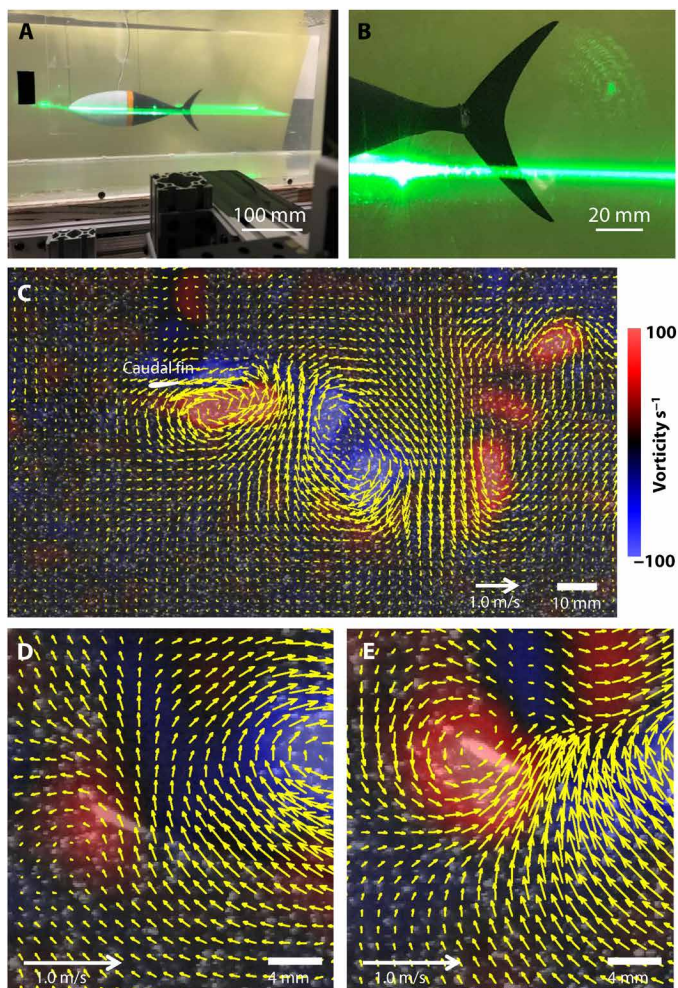
Fig. 7. Visualizing water flow in the wake and around the tail of the Tunabot. The Tunabot body and tail in the laser light sheet (**A**) and a close view of the Tunabot caudal fin with the laser light sheet positioned at the midspan location (**B**). Flow visualization using particle image velocimetry was conducted both in the midbody wake and on the tail surface at the midbody and midspan locations, over the complete range of swimming speeds corresponding to the points shown in Fig. 6. (**C**) A classic reverse Kármán wake is generated by the Tunabot swimming at 0.87 m/s with counter-rotating vortices and high-velocity thrust jets between shed vortex centers. The caudal fin has been highlighted in white. After the start of the tail beat (**D**), a trailing vortex has just been shed from the tail (blue vorticity), and the initial stages of LEV formation can be seen (red, near the tail). Thirteen milliseconds later, during the last half of the tail beat (**E**), a strong LEV is present on the tail (red vorticity). Flows shown in (D) and (E) are at the midspan location. Mean free-stream flow has been subtracted; vorticity scale applies to (C) to (E).

scombrid fishes (*75*, *76*). A generally linear relationship with a positive slope between tail beat frequency and swimming speed is a shared feature of most fishes (*14*, *17*, *30*, *77*), and the Tunabot maintained a speed increase even at the highest tail beat frequencies, suggesting that mechanisms allowing oscillation frequencies above 16 Hz would permit further speed increases.

Through high-speed videography, we observed that the Tunabot achieved swimming kinematics generally similar to those measured for swimming scombrid fishes (Fig. 3), with a wave of bending passing posteriorly along the body, and a fish-like pattern of midline motion that is similar to kinematics of both scombrid (Fig. 3, B and C)

and non-scombrid fishes (*25*, *56*, *78*). However, Tunabot kinematics do show differences from those of scombrid fishes, especially in the region of the caudal fin. Both the relatively high-amplitude curvature that the Tunabot exhibits at 0.8 BL and a reduced curvature in the tail region between 0.8 and 1.0 BL (Fig. 3) differ from scombrid fish kinematics (*75*).

Caudal fin kinematics in fishes are a function of active mechanisms due to actuated motion (side-to-side and angular rotation) at the peduncle and passive effects resulting from body and fin interactions with the water and flexibility of the propulsive surface. The structure of the caudal fin in fishes is composed of a fan of tapered bilaminar fin rays capable of active curvature control (*77*, *78*). Fish fin rays originate at bony plates within the tail and are separated by a thin membrane (*46*, *79*, *80*). This arrangement allows for anisotropic properties, producing stiff and compliant bending axes that we have not replicated in the current Tunabot design. In addition, the Tunabot caudal fin is constructed from a high-stiffness polymer. Relative to biological caudal fins, it can be regarded as an effectively rigid propulsor, and this is reflected in the midline curvatures measured during swimming (Fig. 3A). Future improvements in Tunabot design, which include caudal fin flexibility and the addition of median fins, may improve Tunabot swimming performance by allowing fin-fin and body-fin interactions and enhance caudal fin function as a result of allowing surface deformation. We believe that such improvements are likely to lead to increased swimming performance and result in more fish-like kinematic patterns at the most posterior 20% of the body.

Propulsor stiffness and its influence on fish swimming kinematics have been addressed in a number of previous studies (*79–82*), and here we observed that the flexible caudal fin of swimming tuna and mackerel functions with an average angle of attack that is within an optimal range as estimated from analyses of airfoil function (*57*, *58*). This estimated optimal range for angle of attack of the tail may be a common feature of fish swimming that allows the LEV to be maintained on the tail for a longer period of time than if high angles of attack of the tail occur. At high angles of attack, the LEV will detach (*57*), and this will reduce thrust generated on the tail through leading-edge suction. Tuna, mackerel, and even non-scombrid fishes function within an angle of attack range (*25*, *83*) at which the LEV can be maintained on the tail for much of the tail beat cycle. In species studied experimentally so far, fish caudal fins appear to allow flow separation during the tail beat and to generate an LEV that enhances thrust (*18*, *63*, *84*). Demonstrating the absence or presence of an LEV on the Tunabot tail was a key goal of our flow visualization measurements, and we confirmed both the presence of an LEV and the growth of this LEV as the tail passes through the midline (Fig. 7). Thus, despite some differences between Tunabot and fish tail kinematics, the rigid Tunabot caudal fin with a relatively high effective angle of attack is still able to generate LEVs. The effectiveness of the Tunabot caudal fin in generating an LEV and the action of the tail as a lift (and hence thrust) generating device may be one reason why the Tunabot is able to achieve fish-like swimming performance. However, the rigid tail of the Tunabot achieves angles of attack that are higher than that seen in fishes, and thus, the Tunabot may shed the LEV early compared with fishes and thus may experience reduced thrust and hence a lower stride length compared with freely swimming tuna. Future improvements in Tunabot design may allow an even closer match to fish propulsive systems and may permit extension of fish-like mechanical systems even further into the fish performance space.
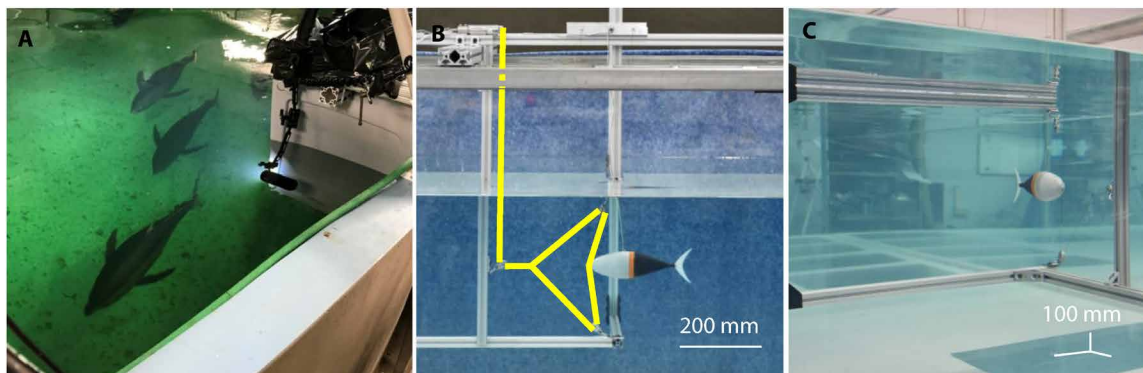
Fig. 8. Measuring swimming performance. (A) High-speed video recording of swimming kinematics in yellowfin tuna. A high-speed camera is suspended above swimming tuna in an enclosed waterproof container (visible in the top right) and provides dorsal views of tuna body deformation during swimming. (**B**) Measuring thrust in the Tunabot. Spectra line (highlighted in yellow) connects the tip of the Tunabot to the load cell through three hinged pulleys. Swimming thrust is directly transferred to the load cell. (**C**) Tunabot suspended in a testing tank. Further information on testing protocols is provided in Materials and Methods and the Supplementary Materials.

MATERIALS AND METHODS

Anatomy of scombrid fishes

Both yellowfin tuna (*T. albacares*) and Atlantic mackerel (*S. scombrus*) are high-performance fishes within the family Scombridae, and we studied the anatomy of both species, as well as other species in this family (see figs. S9 and S10), to provide biological inspiration for constructing the Tunabot. Dissections of fresh specimens of both species were used to identify major anatomical components with a focus on the caudal peduncle region and tail. To provide 3D models of the body, peduncle, and tail regions, we took CT scans (Bruker SkyScan 1173, 6- to 30-μm voxel size, 30 to 80 kV, 120 to 200 mA) of tuna and mackerel and processed these scans in Mimics (v17, Materialise Inc., Belgium). These models were used as a guide in designing the Tunabot body and tail shape. In particular, the lateral keel design of the Tunabot was taken directly from the 3D reconstruction of yellowfin tuna keel shape (Fig. 2, E to G). Images of selected 3D models and 3D prints of yellowfin tuna anatomy are provided in the Supplementary Materials.

Fish and Tunabot swimming kinematics

Swimming kinematics of yellowfin tuna (*T. albacares*) were obtained at the Greenfins Inc. tuna facility (Narragansett, RI, USA) where tuna averaging 1 m in length swam freely in a 473,000-liter, saltwater, circular tank (12.2 m in diameter, water level more than 3 m). This large tank allows for tuna locomotion to be largely unconstrained; fish are free to change direction and maneuver. We recorded both dorsal and lateral video sequences of yellowfin tuna using GoPro4 cameras at 240 frames per second (fps) and Photron Mini AX100 cameras at 250 and 500 fps. Both routine steady swimming at about 1.0 BL/s and high-speed swimming and maneuvering during feeding were recorded. Feeding sequences provided kinematic data over a range of tail beat frequencies up to 10 Hz (e.g., Fig. 5B) as locomotion was more active at this time. We were unable to quantify swimming speed during these high-frequency feeding sequences because tunas were maneuvering rapidly in three dimensions.

We recorded ventral view kinematics of mackerel and the Tunabot in a laboratory flow tank as in previous research (*45*, *85*, *86*) using a Photron Mini UX100 and PCI-1024 high-speed digital video cameras filming at 250 to 1000 fps (snapshots at one time instant are given in the top panels of Fig. 3). Digital videos had a resolution of either 1280 × 1024 pixels (for the UX100 camera) or 1024 × 1024

pixels (for the PCI-1024 camera). Mackerel data were obtained under Harvard animal care protocol 20-03 to G.V.L. Midline kinematics for the Tunabot were recorded from three trials at each of nine tail beat frequencies ranging from 2.47 to 14.78 Hz (0.4 to 4.0 BL/s). Mackerel midline kinematics were recorded during steady swimming at 1, 1.3, and 2 BL/s. We digitized the midlines of tuna, mackerel, and the Tunabot from digital video sequences by manually tracking the midline on 10 evenly spaced frames across a full tail beat cycle using a custom MATLAB program following the procedures outlined in (*45*, *85*). These digitized sequences were then used to calculate tail beat frequency, maximum tail beat amplitude, and midline kinematic oscillations (as shown in Fig. 3).

Tunabot design and fabrication

The Tunabot body consists of eight major components: the head, motor, actuating mechanism, support structure for the actuating mechanism, posterior support structure (with ribs), keeled peduncle, flexible posterior skin, and caudal fin (Fig. 2). The head and internal support structures were 3D-printed in acrylonitrile butadiene styrene (ABS). The keeled peduncle was 3D-printed in stainless steel for strength, whereas the tail was 3D-printed with VeroWhite resin. The Tunabot's external shape was based on a yellowfin tuna body with all fins removed except the tail, and the Tunabot is 255.3 mm in length, 49.2 mm in width, and 67.8 mm in height. It has a mass of 0.306 kg in air. The Tunabot is powered by an Actobotics DC motor (970 RPM Econ Gear Motor; gear ratio, 10:1), which is controlled off-board with a pulse-width modulation (PWM) controller. The motor sits in the 3D-printed, ABS head of the Tunabot, and a drive shaft connects this motor to an actuating mechanism located just posterior to the head section of the Tunabot. This actuating mechanism translates rotation of the drive shaft into lateral linear movement (animation of the mechanism is shown in movie S7). Our waterproofing procedure for the 3D-printed ABS parts that housed electrical components is discussed in the Supplementary Materials. Although no on-board battery was provided in this current iteration of the Tunabot test platform, the head could be modified to include space for a 10-Wh battery pack, which would provide a range of ~9.1 km if the Tunabot swims at 0.4 m/s or ~4.2 km at 1.0 m/s.

Posterior to the head, the actuating system was covered with an elastomer skin, which aided in maintaining a streamlined body similar to scombrid fishes (Fig. 2, B and C), and 3D-printed ribs supporting

the flexible skin on the posterior half of the body. We introduced a tensile prestress of about 5% to the elastomer skin to minimize buckling during actuation, although we were not able to eliminate all buckling at higher actuation frequencies. This elastomer skin covers the posterior Tunabot body and ends before the tail. This skin was custom-designed and cast with Ecoflex Dragon Skin 10 NV (Smooth-On Inc., USA) with a shore hardness of A10. The skin was cast into one continuous funnel-shaped piece using a custom 3D-printed mold to minimize the chance of leakage. Thickness of the skin was 1.5 mm.

Although tunas have many intervertebral joints to allow bending, we chose a simpler, more robust, and more predictable design with fewer joints to create lateral bending in the Tunabot. This lateral bending manifests at two joints—one midbody joint between the actuating mechanism and the posterior support structure and a posterior joint between the lateral-keeled peduncle and the tail. Using CT scans, we found that tunas and mackerel have modified their vertebrae in many ways (enlarged zygapophyses, neural and hemal spines that overlap onto neighboring vertebrae) to prevent dorso-ventral flexion and limit vertebral bending just to the lateral plane. Further images and details are provided in the Supplementary Materials. We therefore similarly constrained motion of the Tunabot's joints so that they could only rotate in the lateral direction and create more fish-like bending. The midbody joint was designed to facilitate the bending operation of the actuation mechanism. It consists of two ball bearing assemblies that reduce friction during bending but maintain structural stability and resist twisting of the body during propulsion. We also passively controlled the posterior joint between the keeled peduncle and tail in two ways: (i) We created physical stops at 18° tail-bending angles to prevent nonbiological bending angles, and (ii) we attached elastic bands between the keeled peduncle and the tail to act like the lateral tendons of tunas and bring the caudal fin back to the neutral position of 0°. The high–aspect ratio tail was inspired by CT scans of tuna tails and was given a chordwise cross section of a NACA 0016 airfoil.

The lateral position of the peduncle flexion is determined by

$$d(t) = L_p \sin(\Phi) \sin \omega t$$

where L_p is the distance between body flexion and peduncle flexion, Φ is the maximum bending angle, and ω is the angular velocity of the motor. For the current design, where $L_p = 89.3$ mm and $\Phi = 16°$, the maximum lateral displacement at the peduncle is 24.6 mm, which is equal to half body width or 0.37 BL. During locomotion, the Tunabot tail encounters fluid resistance that varies with frequency, and hence, tail beat amplitude is not constant as swimming speed increases. Tunabot tail beat amplitude is inversely proportional to the experimental frequency, and the average tail beat amplitudes are 0.18 and 0.13 BL during the minimum and maximum tested tail beat frequencies, respectively. Amplitude data for all frequencies are presented in the Supplementary Materials.

Tunabot performance testing protocol
A custom-built flow tank used in our previous research on fish locomotion (85, 87, 88) was used to test and quantify the performance of the Tunabot. The test section of the flow tank was 28 cm by 28 cm by 66 cm ($W \times H \times L$), and the tank was computer-controlled to generate flows from a few centimeters per second to greater than 1.1 m/s. Our testing conditions were "semi-autonomous" because the constraints

on body positioning were minimal, but the Tunabot required external power input. Two flexible and thin (diameter, ~1 mm) electrical wires exited the Tunabot at about 33% BL and were connected between the DC motor and the PWM off-board controller to provide motor control. Drag force on the wires was estimated and was negligible at slow swimming speeds (Tunabot drag forces are discussed in the Supplementary Materials). These wires were attached in a loose manner so that they were not supporting the weight of the Tunabot (see below). This tethered arrangement simplified the electronics system and reduced experimental time, and we believe that these results are also applicable to a fully autonomous Tunabot of the same design because our constraints on Tunabot position were minimal.

The Tunabot has negative buoyancy, weighing 59 g in water, and lacks control surfaces to adjust turns in yaw or changes in pitch. To encourage straight steady swimming during experiments, we used three cables (two vertical and one lateral) to help control extreme movements in yaw and pitch. We attached two thin, braided, ultrahigh–molecular weight polyethylene (Spectra) lines (Fig. 8B) vertically from the Tunabot body (at 3 and 125 mm from the snout) to a rig over the flow tank. These lines ensured that the negatively buoyant Tunabot was leveled horizontally and that any initial pitch was eliminated. We attached a third laterally placed line between the vertical cable at the nose and the opposite wall to limit extreme yaw motion and prevent unwanted yaw turning of the robot in the event of mechanical failure. No force was applied in the streamwise or lateral directions, and hence, the forces and swimming velocity measured in the experiments are representative of untethered swimming.

To investigate swimming performance of the Tunabot, we measured the self-propelled speed of the Tunabot over nine PWM duty cycles between 20 and 100% in 10% increments. Duty cycles less than 20% were ignored because the Tunabot's motor does not turn over until 14% duty cycle power has been supplied. To begin measuring self-propelled speed, we marked the location of the Tunabot's nose on the outside of flow tank under conditions of zero flow (Fig. 8A). This is referred to as the zero position. At each tail beat frequency tested, the flow speed was adjusted until the nose is at the zero position, indicating that the Tunabot was not experiencing any net thrust or drag forces, and hence is at a self-propelled speed. A Photron high-speed camera (see above) recorded the relative position between the zero position and the vehicle's nose in real time. Photron FASTCAM Viewer software displaying the camera's image allowed zero position detection to within 3 mm; the displayed image had a calibrated length scale, and a digital marker was placed 3 mm downstream of zero position. When zero position was achieved within this range, the Tunabot's swimming speed and the tank's flow speed are equal, and the Tunabot's location is stationary within the test section in the earth frame of reference, reflecting conditions of zero net thrust averaged over a tail beat cycle. At this point, the flow speed was recorded as the Tunabot's self-propelled swimming speed.

Power measurement
Power was calculated by multiplying the voltage and current waveforms at each time point. We found that multiplying the two instantaneous voltage and current signals produced more accurate results than using time averages of the signals to calculate the power. A single National Instruments (NI) USB-6259 device was used with LabVIEW to record the voltage and current signals. The PWM signal

was measured to be 15.09 kHz with an oscilloscope, at a 500-kHz sampling rate sufficient to resolve both the voltage and current signals. The power supply for the PWM controller outputs 12.22 V, such that the PWM square wave ranged from 0 to 12.22 V. The NI USB-6259 is capable of receiving analog input up to 10 V, and a voltage divider composed of two 5.1 kilohms ± 5% resistors was used to halve the 12.22-V PWM signal for recording.

A current transducer, model LAH 25-NP (LEM Electronics, China), converts the current signal between the positive terminals of the motor and PWM controller to a proportional voltage signal, which was then recorded by the NI USB-6259. The LAH 25-NP is a closed-loop, single-channel Hall effect transducer with a frequency bandwidth of 200 kHz. The transducer's 8A wiring configuration encompassed the Tunabot's maximum motor current and provided excellent sensitivity with a turns ratio of 3:1000. A dedicated Agilent E3648A power supply provided two 12-V channels to the transducer.

Voltage and current signals were recorded at 500 kHz for 5 s, yielding 2.5 million data points to describe Tunabot power consumption. Both signals were synchronized during recording to ensure that the voltage and current signals are exactly in phase, which is essential for the power calculation. The 5-s collection window ensures that the power is averaged over 12 to 74 complete tail beat periods of the Tunabot depending on the swimming speed.

MATLAB software (MathWorks Inc., Natick, MA, USA) was used to calculate the average power from the raw voltage and current signal data. Before this was done, the raw data were filtered and corrected. A median filter was applied to the voltage data to isolate the square wave PWM signal. As explained previously, the 12.22-V PWM voltage signal was halved before being recorded because of the 10-V limitation of the NI USB-6259, so the voltage data were rescaled such that it ranged from 0 to 12.22 V. This is known to be the original PWM signal's range based on an oscilloscope reading and the 12.22-V power supply of the PWM controller. The current data were also filtered in a similar manner to the voltage signals. A cubic-weighted Savitzky-Golay filter was applied to the current data. We used the smallest frame length possible (five points) to eliminate noise and minimally smooth the meaningful data points. After voltage and current were filtered and corrected, the two were multiplied together to calculate the power with respect to time. Last, the mean power was found by taking the average of these points over the 5-s collection window.

Thrust measurement

Thrust produced by the Tunabot was measured using a custom-built rig (Fig. 8, B and C) in a stationary water tank of 1.5 m by 0.9 m by 4.7 m ($W \times H \times L$). The Tunabot was suspended using the same setup as in the flow tank (see the "Tunabot performance testing protocol" section) with one difference: No lateral string was used to control transverse movement of the Tunabot because stationary water did not create unwanted transverse movement. Thrust was measured using an Omegadyne LC601-1 (serial number 278001) load cell. The load cell was connected to the tip of the Tunabot's head by a string that ran through three pulleys that transferred the Tunabot's forward thrust to the load cell. The pulleys were arranged in a triangle such that the force transfer was one to one and only the forward thrust component was transferred. All pulleys were attached with three degrees of freedom and therefore did not restrict the motion of the Tunabot. The Tunabot's motions in the flow tank, especially oscillatory transverse motion, were observed in the stationary thrust rig. The output

voltage of the load cell passed through an Omega DMD4059 signal conditioner before being recorded by an NI USB-6008 device with LabVIEW. We measured thrust over three trials spanning 0 to 100% PWM duty cycle by 10% increments excluding 10%, which is too small to turn the motor. A 0% duty cycle was measured to zero the thrust measurement, and this zero thrust was subtracted from non-zero duty cycle measurements. Power was measured simultaneously with the thrust using the same methodology as described previously. Between each trial, we removed and replaced the Tunabot's caudal fin and skin to account for measurement error due to changes in skin tension and reassembly.

Flow visualization

Tunabot flow visualization was measured in a laboratory flow tank using a Photron Mini UX100 high-speed camera at a speed of 1000 fps with a resolution of 1280 × 1024 pixels. As in our previous research (20, 45, 89, 90), small particles (mean size, 50 μm) were introduced into the flow, and an Opto Engine 5-W argon ion laser in conjunction with a Powell lens generated a horizontal light sheet directed at the Tunabot (Fig. 7, A and B). DaVis 8.4 software (LaVision Inc., Göttingen, Germany) was used to process pairs of sequential video frames to generate a time series of velocity vector fields throughout the tail beat cycle. Images of the flow field generated by the swimming Tunabot were taken both at the horizontal body midline (Fig. 7A) and at the midcaudal span location (Fig. 7B).

SUPPLEMENTARY MATERIALS

robotics.sciencemag.org/cgi/content/full/4/34/eaax4615/DC1

Text
Fig. S1. Internal structure of fusion deposition modeling (FDM) 3D-printed materials with different part fill densities.
Fig. S2. Elastomer infiltration for a 3D-printed material.
Fig. S3. Airtight testing of an elastomer-infiltrated 3D-printed closed chamber.
Fig. S4. Kinematic and lift-based swimming principles.
Fig. S5. Drag force on a wire in a steady fluid flow.
Fig. S6. Drag versus flow speed for the Tunabot body.
Fig. S7. Tunabot body drag coefficients.
Fig. S8. Tunabot head and tail oscillation amplitude.
Fig. S9. Scombrid fish 3D anatomy.
Fig. S10. Scombrid fish 3D anatomy.
Table S1. Data used for Fig. 1: Fish and robot locomotor performance space.
Movie S1. Yellowfin tuna steady swimming.
Movie S2. Atlantic mackerel steady swimming.
Movie S3. Tunabot swimming in a flow tank.
Movie S4. Tunabot swimming in laser light sheet.
Movie S5. Wide view of Tunabot wake flow patterns.
Movie S6. Close view of Tunabot wake flow visualization around the caudal fin.
Movie S7. Animation of the Tunabot propulsive mechanism.
References (91–93)

REFERENCES AND NOTES

1. R. K. Katzschmann, J. DelPreto, R. MacCurdy, D. Rus, Exploration of underwater life with an acoustically controlled soft robotic fish. *Sci. Robot.* **3**, eaar3449 (2018).
2. F. Gibouin, C. Raufaste, Y. Bouret, M. Argentina, Study of the thrust–drag balance with a swimming robotic fish. *Phys. Fluids* **30**, 091901 (2018).
3. R. Du, Z. Li, K. Youcef-Toumi, P. Valdivia y Alvarado, Eds., *Robot Fish. Bio-Inspired Fishlike Underwater Robots* (Springer Verlag, Berlin, 2015).
4. J. H. Long Jr., T. J. Koob, K. Irving, K. Combie, V. Engel, N. Livingston, A. Lammert, J. Schumacher, Biomimetic evolutionary analysis: Testing the adaptive value of vertebrate tail stiffness in autonomous swimming robots. *J. Exp. Biol.* **209**, 4732–4746 (2006).
5. X. Tan, D. Kim, N. Usher, D. Laboy, J. Jackson, A. Kapetanovic, J. Rapai, B. Sabadus, X. Zhou, An autonomous robotic fish for mobile sensing, in *Proceedings of the IEEE/RSJ International Conference on Intelligent Robots and Systems* (IEEE, Beijing, China, 2006), pp. 5424–5429.
6. M. Kruusmaa, P. Fiorini, W. Megill, M. de Vittorio, O. Akanyeti, F. Visentin, L. Chambers, H. E. Daou, M.-C. Fiazza, J. Ježov, M. Listak, L. Rossi, T. Salumae, G. Toming, R. Venturelli,

D. S. Jung, J. Brown, F. Rizzi, A. Qualtieri, J. L. Maud, A. Liszewski, FILOSE for svenning: A flow sensing bioinspired robot. *IEEE Robot. Autom. Mag.* **21**, 51–62 (2014).

7. M. Rufo, M. Smithers, GhostSwimmer™ AUV: Applying biomimetics to underwater robotics for achievement of tactical relevance. *Mar. Technol. Soc. J.* **45**, 24–30 (2011).

8. G. V. Lauder, J. Lim, R. Shelton, C. Witt, E. J. Anderson, J. L. Tangorra, Robotic models for studying undulatory locomotion in fishes. *Mar. Technol. Soc. J.* **45**, 41–55 (2011).

9. G. V. Lauder, J. L. Tangorra, Fish locomotion: Biology and robotics of body and fin-based movements, in *Robot Fish. Bio-inspired Fishlike Underwater Robots*, R. Du, Z. Li, K. Youcef-Toumi, P. Valdivia y Alvarado, Eds. (Springer Verlag, Berlin, 2015), pp. 25–49.

10. J. L. Tangorra, G. V. Lauder, I. W. Hunter, R. Mittal, P. G. A. Madden, M. Bozkurttas, The effect of fin ray flexural rigidity on the propulsive forces generated by a biorobotic fish pectoral fin. *J. Exp. Biol.* **213**, 4043–4054 (2010).

11. J. C. Kahn Jr., D. J. Peretz, J. L. Tangorra, Predicting propulsive forces using distributed sensors in a compliant, high DOF, robotic fin. *Bioinspir. Biomim.* **10**, 036009 (2015).

12. M. C. Leftwich, E. D. Tytell, A. H. Cohen, A. J. Smits, Wake structures behind a swimming robotic lamprey with a passively flexible tail. *J. Exp. Biol.* **215**, 416–425 (2012).

13. J. J. Videler, C. S. Wardle, Fish swimming stride by stride: Speed limits and endurance. *Rev. Fish Biol. Fisher.* **1**, 23–40 (1991).

14. R. Bainbridge, The speed of swimming of fish as related to size and to the frequency and amplitude of the tail beat. *J. Exp. Biol.* **35**, 109–133 (1958).

15. P. W. Webb, Hydrodynamics and energetics of fish propulsion. *Bull. Fish. Res. Bd. Can.* **190**, 1–159 (1975).

16. J. J. Magnuson, Locomotion by scombrid fishes: Hydromechanics, morphology, and behavior, in *Fish Physiology. Vol. VII. Locomotion*, W. S. Hoar, D. J. Randall, Eds. (Academic Press, New York, 1978), pp. 239–313.

17. J. R. Hunter, J. R. Zweifel, Swimming speed, tail beat frequency, tail beat amplitude, and size in jack mackerel, *Trachurus symmetricus*, and other fishes. *Fish. Bull.* **69**, 253–266 (1971).

18. N. Gravish, G. V. Lauder, Robotics-inspired biology. *J. Exp. Biol.* **221**, 138438 (2018).

19. G. V. Lauder, Fish locomotion: Recent advances and new directions. *Ann. Rev. Mar. Sci.* **7**, 521–545 (2015).

20. J. C. Nauen, G. V. Lauder, Hydrodynamics of caudal fin locomotion by chub mackerel, *Scomber japonicus* (Scombridae). *J. Exp. Biol.* **205**, 1709–1724 (2002).

21. U. K. Müller, B. van den Heuvel, E. J. Stamhuis, J. J. Videler, Fish foot prints: Morphology and energetics of the wake behind a continuously swimming mullet (*Chelon labrosus* Risso). *J. Exp. Biol.* **200**, 2893–2906 (1997).

22. E. D. Tytell, G. V. Lauder, The hydrodynamics of eel swimming: I. Wake structure. *J. Exp. Biol.* **207**, 1825–1841 (2004).

23. M. J. Lighthill, Hydromechanics of aquatic animal propulsion. *Ann. Rev. Fluid Mech.* **1**, 413–446 (1969).

24. U. K. Müller, E. J. Stamhuis, J. J. Videler, Riding the waves: The role of the body wave in undulatory fish swimming. *Integr. Comp. Biol.* **42**, 981–987 (2002).

25. B. C. Jayne, G. V. Lauder, Speed effects on midline kinematics during steady undulatory swimming of largemouth bass, *Micropterus salmoides*. *J. Exp. Biol.* **198**, 585–602 (1995).

26. G. B. Gillis, Undulatory locomotion in elongate aquatic vertebrates: Anguilliform swimming since Sir. James Gray. *Amer. Zool.* **36**, 656–665 (1996).

27. J. D. Altringham, D. J. Ellerby, Fish swimming: Patterns in muscle function. *J. Exp. Biol.* **202**, 3397–3403 (1999).

28. J. C. Liao, Swimming in needlefish (Belonidae): Anguilliform locomotion with fins. *J. Exp. Biol.* **205**, 2875–2884 (2002).

29. N. Nangia, R. Bale, N. Chen, Y. Hanna, N. A. Patankar, Optimal specific wavelength for maximum thrust production in undulatory propulsion. *PLOS ONE* **12**, e0179727 (2017).

30. H. Dewar, J. B. Graham, Studies of tropical tuna swimming performance in a large water tunnel - kinematics. *J. Exp. Biol.* **192**, 45–59 (1994).

31. C. J. Esposito, J. L. Tangorra, B. E. Flammang, G. V. Lauder, A robotic fish caudal fin: Effects of stiffness and motor program on locomotor performance. *J. Exp. Biol.* **215**, 56–67 (2012).

32. J. R. Gottlieb, J. L. Tangorra, C. J. Esposito, G. V. Lauder, A biologically derived pectoral fin for yaw turn manoeuvres. *Appl. Bionics Biomech.* **7**, 41–55 (2010).

33. M. C. Leftwich, A. J. Smits, Thrust production by a mechanical swimming lamprey. *Exp. Fluids* **50**, 1349–1355 (2011).

34. M. A. MacIver, E. Fontaine, J. W. Burdick, Designing future underwater vehicles: Principles and mechanisms of the weakly electric fish. *IEEE J. Oceanic Eng.* **29**, 651–659 (2004).

35. J. H. Long Jr., J. Schumacher, N. Livingston, M. Kemp, Four flippers or two? Tetrapodal swimming with an aquatic robot. *Bioinspir. Biomim.* **1**, 20–29 (2006).

36. K. W. Moored, F. E. Fish, T. H. Kemp, H. Bart-Smith, Batoid fishes: Inspiration for the next generation of underwater robots. *Mar. Tech. Soc. J.* **45**, 99–109 (2011).

37. J. Tangorra, C. Phelan, C. Esposito, G. Lauder, Use of biorobotic models of highly deformable fins for studying the mechanics and control of fin forces in fishes. *Integr. Comp. Biol.* **51**, 176–189 (2011).

38. G. V. Lauder, B. E. Flammang, S. Alben, Passive robotic models of propulsion by the bodies and caudal fins of fish. *Integr. Comp. Biol.* **52**, 576–587 (2012).

39. J. M. Anderson, N. Chhabra, Maneuvering and stability performance of a robotic tuna. *Integr. Comp. Biol.* **42**, 118–126 (2002).

40. T. Li, G. Li, Y. Liang, T. Cheng, J. Dai, X. Yang, B. Liu, Z. Zeng, Z. Huang, Y. Luo, T. Xie, W. Yang, Fast-moving soft electronic fish. *Sci. Adv.* **3**, e1602045 (2017).

41. C. Christianson, N. N. Goldberg, D. D. Deheyn, S. Cai, M. T. Tolley, Translucent soft robots driven by frameless fluid electrode dielectric elastomer actuators. *Sci. Robot.* **3**, eaat1893 (2018).

42. O. M. Curet, N. A. Patankar, G. V. Lauder, M. A. MacIver, Mechanical properties of a bio-inspired robotic knifefish with an undulatory propulsor. *Bioinspir. Biomim.* **6**, 026004 (2011).

43. S. McGovern, G. Alici, V.-T. Truong, G. Spinks, Finding NEMO (novel electromaterial muscle oscillator): A polypyrrole powered robotic fish with real-time wireless speed and directional control. *Smart Mater. Struct.* **18**, 095009 (2009).

44. S. Fujiwara, S. Yamaguchi, Development of fishlike robot that imitates carangiform and subcarangiform swimming motions. *J. Aero Aqua Bio-Mechanisms* **6**, 1–8 (2017).

45. R. M. Shelton, P. J. M. Thornycroft, G. V. Lauder, Undulatory locomotion of flexible foils as biomimetic models for understanding fish propulsion. *J. Exp. Biol.* **217**, 2110–2120 (2014).

46. I. D. Neveln, Y. Bai, J. B. Snyder, J. R. Solberg, O. M. Curet, K. M. Lynch, M. A. MacIver, Biomimetic and bio-inspired robotics in electric fish research. *J. Exp. Biol.* **216**, 2501–2514 (2013).

47. R. E. Shadwick, D. A. Syme, Thunniform swimming: Muscle dynamics and mechanical power production of aerobic fibres in yellowfin tuna (*Thunnus albacares*). *J. Exp. Biol.* **211**, 1603–1611 (2008).

48. H. L. Fierstine, V. Walters, Studies in locomotion and anatomy of scombroid fishes. *Mem. So. Cal. Acad. Sci.* **6**, 1–31 (1968).

49. J. B. Graham, K. A. Dickson, The evolution of thunniform locomotion and heat conservation in scombrid fishes: New insights based on the morphology of *Allothunnus fallai*. *Zool. J. Linn. Soc. Lond.* **129**, 419–466 (2000).

50. K. A. Dickson, J. Graham, Evolution and consequences of endothermy in fishes. *Physiol. Biochem. Zool.* **77**, 998–1018 (2004).

51. B. Block, E. D. Stevens, Eds., *Tuna: Physiology, Ecology, and Evolution* (Academic Press, San Diego, 2001), vol. 19.

52. M. Westneat, S. A. Wainwright, Mechanical design for swimming: Muscle, tendon, and bone in *Tuna: Physiology, Ecology, and Evolution,* B. A. Block, E. D. Stevens, Eds. (Academic Press, San Diego, 2001), pp. 271–311.

53. T. Knower, R. E. Shadwick, A. A. Biewener, K. Korsmeyer, J. B. Graham, Direct measurement of tail tendon forces in swimming tuna. *Am. Zool.* **3**, 30A (1993).

54. J. J. Videler, F. Hess, Fast continuous swimming of two pelagic predators, saithe (*Pollachius virens*) and mackerel (*Scomber scombrus*): A kinematic analysis. *J. Exp. Biol.* **109**, 209–228 (1984).

55. S. L. Katz, R. E. Shadwick, Curvature of swimming fish midlines as an index of muscle strain suggests swimming muscle produces net positive work. *J. Theor. Biol.* **193**, 243–256 (1998).

56. R. Shadwick, S. Gemballa, Structure, kinematics, and muscle dynamics in undulatory swimming, in *Fish Biomechanics. Volume 23 in Fish Physiology*, R. E. Shadwick, G. V. Lauder, Eds. (Academic Press, San Diego, 2006), pp. 241–280.

57. M. Raffel, J. Kompenhans, P. Wernert, Investigation of the unsteady flow velocity field above an airfoil pitching under deep dynamic stall conditions. *Exp. Fluids* **19**, 103–111 (1995).

58. L. M. Lourenco, A. Krothapalli, L. Van Dommelen, C. Shih, Unsteady flow past a NACA 0012 airfoil pitching at constant rates. *Defense Technical Information Center* **AD-A265159**, 1–83 (1993).

59. M. H. Dickinson, Unsteady mechanisms of force generation in aquatic and aerial locomotion. *Am. Zool.* **36**, 537–554 (1996).

60. M. H. Dickinson, F.-O. Lehmann, S. Sane, Wing rotation and the aerodynamic basis of insect flight. *Science* **284**, 1954–1960 (1999).

61. C. P. Ellington, C. van den Berg, A. P. Willmott, A. L. R. Thomas, Leading-edge vortices in insect flight. *Nature* **384**, 626–630 (1996).

62. D. Lentink, F. T. Muijres, F. J. Donker-Duyvis, J. L. van Leeuwen, Vortex-wake interactions of a flapping foil that models animal swimming and flight. *J. Exp. Biol.* **211**, 267–273 (2008).

63. I. Borazjani, M. Daghooghi, The fish tail motion forms an attached leading edge vortex. *Proc. Biol. Sci.* **280**, 20122071 (2013).

64. J. M. Blank, C. J. Farwell, J. M. Morrissette, R. J. Schallert, B. A. Block, Influence of swimming speed on metabolic rates of juvenile Pacific bluefin tuna and yellowfin tuna. *Physiol. Biochem. Zool.* **80**, 167–177 (2007).

65. V. Di Santo, C. P. Kenaley, G. V. Lauder, High postural costs and anaerobic metabolism during swimming support the hypothesis of a U-shaped metabolism–speed curve in fishes. *Proc. Natl. Acad. Sci. U.S.A.* **114**, 13048–13053 (2017).

66. G. K. Taylor, R. L. Nudds, A. L. R. Thomas, Flying and swimming animals cruise at a Strouhal number tuned for high power efficiency. *Nature* **425**, 707–711 (2003).

67. C. Sepulveda, K. A. Dickson, Maximum sustainable speeds and cost of swimming in juvenile Kawakawa tuna (*Euthynnus affinis*) and chub mackerel (*Scomber japonicus*). *J. Exp. Biol.* **203**, 3089–3101 (2000).

68. C. A. Sepulveda, K. A. Dickson, J. B. Graham, Swimming performance studies on the eastern Pacific bonito *Sarda chiliensis*, a close relative of the tunas (family Scombridae) I. Energetics. *J. Exp. Biol.* **206**, 2739–2748 (2003).

69. V. Di Santo, C. P. Kenaley, Skating by: Low energetic costs of swimming in a batoid fish. *J. Exp. Biol.* **219**, 1804–1807 (2016).

70. K. E. Korsmeyer, J. F. Steffensen, J. Herskin, Energetics of median and paired fin swimming, body and caudal fin swimming, and gait transition in parrotfish (*Scarus schlegeli*) and triggerfish (*Rhinecanthus aculeatus*). *J. Exp. Biol.* **205**, 1253–1263 (2002).

71. G. V. Lauder, E. D. Tytell, Hydrodynamics of undulatory propulsion, in *Fish Biomechanics. Volume 23 in Fish Physiology*, R. E. Shadwick, G. V. Lauder, Eds. (Academic Press, San Diego, 2006), pp. 425–468.

72. M. S. Triantafyllou, G. S. Triantafyllou, An efficient swimming machine. *Sci. Am.* **272**, 64–70 (1995).

73. M. S. Triantafyllou, G. S. Triantafyllou, D. K. P. Yue, Hydrodynamics of fishlike swimming. *Ann. Rev. Fluid Mech.* **32**, 33–53 (2000).

74. M. Saadat, F. E. Fish, A. G. Domel, V. Di Santo, G. V. Lauder, H. Haj-Hariri, On the rules for aquatic locomotion. *Phys. Rev. Fluids* **2**, 083102 (2017).

75. A. C. Gibb, K. A. Dickson, G. V. Lauder, Tail kinematics of the chub mackerel *Scomber japonicus*: Testing the homocercal tail model of fish propulsion. *J. Exp. Biol.* **202**, 2433–2447 (1999).

76. J. M. Donley, K. A. Dickson, Swimming kinematics of juvenile Kawakawa tuna (*Euthynnus affinis*) and chub mackerel (*Scomber japonicus*). *J. Exp. Biol.* **203**, 3103–3116 (2000).

77. P. W. Webb, Hydrodynamics: Non-scombroid, in *Fish Physiology. Vol. VII. Locomotion*, W. S. Hoar, D. J. Randall, Eds. (Academic Press, New York, 1978), pp. 189–237.

78. G. V. Lauder, Locomotion, in *The Physiology of Fishes*, D. H. Evans, J. B. Claiborne, Eds. (CRC Press, Boca Raton, ed. 3, 2006), pp. 3–46.

79. J. H. Long Jr., K. S. Nipper, The importance of body stiffness in undulatory propulsion. *Am. Zool.* **36**, 678–694 (1996).

80. J. H. Long, Muscles, elastic energy, and the dynamics of body stiffness in swimming eels. *Am. Zool.* **38**, 771–792 (1998).

81. E. D. Tytell, J. A. Carr, N. Danos, C. Wagenbach, C. M. Sullivan, T. Kiemel, N. J. Cowan, M. M. Ankarali, Body stiffness and damping depend sensitively on the timing of muscle activation in lampreys. *Integr. Comp. Biol.* **58**, 860–873 (2018).

82. E. D. Tytell, C.-Y. Hsu, T. L. Williams, A. H. Cohen, L. J. Fauci, Interactions between internal forces, body stiffness, and fluid environment in a neuromechanical model of lamprey swimming. *Proc. Natl. Acad. Sci. U.S.A.* **107**, 19832–19837 (2010).

83. G. B. Gillis, Anguilliform locomotion in an elongate salamander (*Siren intermedia*): Effects of speed on axial undulatory movements. *J. Exp. Biol.* **200**, 767–784 (1997).

84. D. D. Chin, D. Lentink, Flapping wing aerodynamics: From insects to vertebrates. *J. Exp. Biol.* **219**, 920–932 (2016).

85. G. Xiong, G. V. Lauder, Center of mass motion in swimming fish: Effects of speed and locomotor mode during undulatory propulsion. *Fortschr. Zool.* **117**, 269–281 (2014).

86. E. L. Blevins, G. V. Lauder, Rajiform locomotion: Three-dimensional kinematics of the pectoral fin surface during swimming in the freshwater stingray *Potamotrygon orbignyi*. *J. Exp. Biol.* **215**, 3231–3241 (2012).

87. E. G. Drucker, G. V. Lauder, Locomotor forces on a swimming fish: Three-dimensional vortex wake dynamics quantified using digital particle image velocimetry. *J. Exp. Biol.* **202**, 2393–2412 (1999).

88. V. Di Santo, E. L. Blevins, G. V. Lauder, Batoid locomotion: Effects of speed on pectoral fin deformation in the little skate, *Leucoraja erinacea*. *J. Exp. Biol.* **220**, 705–712 (2017).

89. E. G. Drucker, G. V. Lauder, A hydrodynamic analysis of fish swimming speed: Wake structure and locomotor force in slow and fast labriform swimmers. *J. Exp. Biol.* **203**, 2379–2393 (2000).

90. E. G. Drucker, G. V. Lauder, Locomotor function of the dorsal fin in teleost fishes: Experimental analysis of wake forces in sunfish. *J. Exp. Biol.* **204**, 2943–2958 (2001).

91. G. I. Taylor, Analysis of the swimming of long and narrow animals. *Proc. R. Soc. Lond. A* **214**, 158–183 (1952).

92. D. J. Tritton, *Physical Fluid Dynamics* (Clarendon Press, Oxford, ed. 2, 1988).

93. R. W. Blake, *Fish Locomotion* (Cambridge Univ. Press, Cambridge, 1983).

Citation: J. Zhu, C. White, D. K. Wainwright, V. Di Santo, G. V. Lauder, H. Bart-Smith, Tuna robotics: A high-frequency experimental platform exploring the performance space of swimming fishes. *Sci. Robot.* **4**, eaax4615 (2019).

Tuna robotics: A high-frequency experimental platform exploring the performance space of swimming fishes

J. Zhu, C. White, D. K. Wainwright, V. Di Santo, G. V. Lauder, and H. Bart-Smith

View the article online
https://www.science.org/doi/10.1126/scirobotics.aax4615
Permissions
https://www.science.org/help/reprints-and-permissions

Use of this article is subject to the Terms of service